REFERENCES

[1] Y. Rahmat-Samii, A. Zaghloul, and A. Williams, "Large deployable antennas for satellite communications," in *Proc. IEEE Antennas and Propagation Society Int. Symp.*, 2000, vol. 2, pp. 528–529.

[2] A. R. Cherrete, R. Acosta, P. T. Lam, and S. W. Lee, "Compensation of reflector antenna surface distortion using an array feed," *IEEE Trans. Antennas Propag.*, vol. 37, no. 8, pp. 966–978, 1989.

[3] W. Imbriale, "Distortion compensation techniques for large reflector antennas," in *Proc. IEEE Aerospace Conf.*, 2001, vol. 2, pp. 2/799–2/805.

[4] C. E. Mayer, J. H. Davis, W. L. Petersw, and W. J. Vogel, "A holographic surface measurement of the texas 4.9-meter antenna at 86 ghz," *IEEE Trans. Instrum. Meas.*, vol. IM-32, pp. 102–109, 1983.

[5] Y. Rahmat-Samii and J. Lemanczyk, "Application of spherical near-field measurements to microwave holographic diagnosis of antennas," *IEEE Trans. Antennas Propag.*, vol. 36, no. 6, pp. 869–878, 1988.

[6] J. A. Martinez-Lorenzo, C. M. Rappaport, and A. G. Pino, "Reflector antenna distortion: An iterative-field-matrix solution.," *Radio Sci.*, 2008, 43, RS4019, doi:10.1029/2007RS003813.

[7] W. T. Smith and W. L. Stutzman, "A pattern synthesis technique for array feeds to improve radiation performance of large distorted reflector antennas," *IEEE Trans. Antennas Propag.*, vol. 40, no. 1, pp. 57–62, 1992.

[8] V. Jamnejad and W. Imbriale, "On reflector surface compensation by minimal probing of subreflector field in dual reflector antennas," in *Proc. 2nd Eur. Conf. on Antennas and Propagation EuCAP*, 2007, pp. 1–5.

[9] L. Pereira and J. Bergmann, "Radiation pattern control by subreflector shaping," in *Proc. IEEE Antennas and Propagation Society Int. Symp.*, 2002, vol. 1, pp. 674–677, vol.1.

[10] R. A. Hoferer and Y. Rahmat-Samii, "Subreflector shaping for antenna distortion compensation: An efficient Fourier-Jacobi expansion with GO/PO analysis," *IEEE Trans. Antennas Propag.*, vol. 50, no. 12, pp. 1676–1687, 2002.

[11] B. Gonzalez-Valdes, J. A. Martinez-Lorenzo, C. Rappaport, and A. G. Pino, "Non iterative subreflector shaping for reflector antenna distortion compensation," in *Proc. 4th Eur. Conf. Antennas and Propagation (EuCAP)*, 2010, pp. 1–5.

[12] A. M. Arias, J. O. Rubiños, I. Cuiñas, and A. G. Pino, "Electromagnetic scattering of reflector antennas by fast physical optics algorithms," *Recent Res. Devel. Magn.*, no. 1, pp. 43–63, 2000.

[13] Y. T. Lo and S. W. Lee, *Antenna Handbook*. New York: Van Nostrand Reinhold, 1993, vol. 2.

[14] P. Hansen, "Regularization tools: A Matlab package for analysis and solution of discrete ill-posed problems," *Numer. Algo.*, no. 6, pp. 1–35, 1994.

[15] B. Gonzalez-Valdes, J. Martinez-Lorenzo, C. Rappaport, and A. Pino, "Generating contoured beams with single-shaped reflectors using a iterative field-matrix approach," *IEEE Antennas Wireless Propag. Lett.*, vol. 7, pp. 697–700, 2008.

[16] J. A. Martinez-Lorenzo, B. Gonzalez-Valdes, C. Rappaport, J. Gutierrez-Meana, and A. Garcia Pino, "Reconstructing distortions on reflector antennas with the iterative-field-matrix method using near-field observation data," *IEEE Trans. Antennas Propag.*, vol. 59, no. 6, pp. 2434–2437, 2011.

[17] C. C. Paige and M. A. Saunders, "LSQR: An algorithm for sparse linear equations and sparse least squares," *ACM Trans. Math. Software*, vol. 8, pp. 43–71, 1982.

[18] J. Bergmann, F. Hasselmann, F. Teixeira, and C. Rego, "A comparison between techniques for global surface interpolation in shaped reflector analysis," *IEEE Trans. Antennas Propag.*, vol. 42, no. 1, pp. 47–53, Jan. 1994.

[19] M. Katow, I. Khan, and W. Williams, "Deformable subreflector computed by geometric optics," *Telecommun. Data Acquisition Rep.*, pp. 65–78, 1983.

Incorporation of Exact Boundary Conditions into a Discontinuous Galerkin Finite Element Method for Accurately Solving 2D Time-Dependent Maxwell Equations

Kostyantyn Sirenko, Meilin Liu, and Hakan Bağcı

***Abstract*—A scheme that discretizes exact absorbing boundary conditions (EACs) to incorporate them into a time-domain discontinuous Galerkin finite element method (TD-DG-FEM) is described. The proposed TD-DG-FEM with EACs is used for accurately characterizing transient electromagnetic wave interactions on two-dimensional waveguides. Numerical results demonstrate the proposed method's superiority over the TD-DG-FEM that employs approximate boundary conditions and perfectly matched layers. Additionally, it is shown that the proposed method can produce the solution with ten-eleven digit accuracy when high-order spatial basis functions are used to discretize the Maxwell equations as well as the EACs.**

***Index Terms*—Exact absorbing boundary conditions, numerical analysis, time domain analysis, time domain discontinuous Galerkin finite element method, waveguides.**

I. INTRODUCTION

Time-domain discontinuous Galerkin finite element methods (TD-DG-FEMs), which have recently gained popularity among computational electromagnetics practitioners, are becoming an attractive alternative to finite difference time domain (FDTD) methods in characterization of transient electromagnetic wave interactions [1]–[7]. Unlike "traditional" FEM, DG-FEM utilizes numerical flux to realize "information flow" between discretization elements; use of numerical flux results in localized spatial operations. This equips DG-FEM with several desired properties: (i) Mass matrix is block diagonal and can be inverted with little cost. (ii) Higher-order spatial basis functions and adaptive/hybrid meshing schemes are easily implemented. (iii) Time integration/marching is explicit.

On the other hand, like all other differential equation based solution techniques, DG-FEM requires an unbounded physical domain of interest to be truncated into a bounded computation domain. The most well known technique used for this purpose is to introduce a perfectly matched layer (PML) around the computation domain [8], [9]; DG-FEMs that utilize PML have already been developed [3], [5]. Despite being error-controllable (up to certain degree), PMLs give rise to non-negligible errors, which tend to accumulate during long-duration simulations. Additionally, it has been recently shown that low-order PML profiles work considerably better than high-order ones when incorporated in DG-FEM [5]. This means that when DG-FEM is used for characterizing wave interactions in unbounded

Manuscript received December 21, 2011; revised August 30, 2012; accepted September 17, 2012. Date of publication September 21, 2012; date of current version December 28, 2012. This work was supported in part by an Academic Excellence Alliance program award from the King Abdullah University of Science and Technology (KAUST) Global Collaborative Research under the title "Energy Efficient Photonic and Spintronic Devices" and in part by the Center for Uncertainty Quantification in Computational Science and Engineering at KAUST.

The authors are with the Division of Computer, Electrical and Mathematical Sciences and Engineering, King Abdullah University of Science and Technology (KAUST), Thuwal, 23955-6900, Kingdom of Saudi Arabia (e-mail: hakan.bagci@kaust.edu.sa).

Color versions of one or more of the figures in this communication are available online at http://ieeexplore.ieee.org.

Digital Object Identifier 10.1109/TAP.2012.2220102

domains truncated by PML, increasing the order of the spatial basis functions will not result in a more accurate solution, i.e., the overall accuracy of the simulation will be limited by the accuracy of the PML. Use of mathematically exact absorbing boundary conditions (EACs) could be greatly beneficial in such cases. There are several well-developed approaches to EACs, which have been extensively used with traditional FEM and FDTD [6], [7], [10]–[13], but there are only a few publications on DG-FEM with EACs, and these publications do not provide details about the discretization of the EACs and the incorporation of the discretized forms into the DG-FEM framework [6], [7].

In this work, time-domain EAC, which has been previously used in FDTD frameworks [10]–[13], is combined with high-order TD-DG-FEM for solving Maxwell equations to characterize transient wave interactions on two-dimensional (2D) waveguides. The EAC under consideration is analytically derived from the radiation conditions of the outgoing waves. It should be noted here that the EACs used here are different than those in [6], [7]. The latter are obtained through the application of an iterative procedure to the radiation conditions and are only asymptotically exact. Additionally, their incorporation into the TD-DG-FEM framework requires introduction of auxiliary variables. Furthermore, this work explains in detail how the EACs can be discretized using a high-order scheme that is fully consistent with the discretization scheme employed by the TD-DG-FEM. This approach ensures that the accuracy of the EAC discretization matches that of the TD-DG-FEM for all orders of spatial basis functions. Numerical results demonstrate the superiority of the proposed method over the TD-DG-FEM that employs approximate boundary conditions and PML. It is also shown that the TD-DG-FEM with EAC can produce the solution with ten-eleven digit accuracy when high-order spatial basis functions are used to discretize the Maxwell equations as well as the EAC.

II. Formulation

A. Maxwell Equations and Their Discretization

Consider the 2D waveguide shown in Fig. 1. Here, $\Omega = \Omega_L \cup \mathbf{I} \cup \mathbf{II} \cup \mathbf{L}_1 \cup \mathbf{L}_2$ is the unbounded source-free physical domain, Ω_L is the bounded computation domain, $\mathbf{I} = \{\mathbf{r} \in \Omega : z < L_1\}$ and $\mathbf{II} = \{\mathbf{r} \in \Omega : z > L_2\}$ are the homogeneous external regions, and $\mathbf{L}_j = \{\mathbf{r} \in \Omega : z = L_j\}, j \in \{1, 2\}$ are the virtual boundaries between Ω_L and $\mathbf{I}$ and $\mathbf{II}$, respectively. Here, $\mathbf{r} = (y, z)$, $\mathbf{r} \in \Omega$, is the location vector in 2D Cartesian coordinates. S^{PEC} represents surfaces of all perfect electrically conducting (PEC) objects. It is assumed that all material inhomogeneities are located within Ω_L. Transverse electric field (TE) wave interactions in Ω are governed by the time-dependent Maxwell equations:

$$\begin{aligned}
\varepsilon(\mathbf{r})\partial_t E_x(\mathbf{r},t) &= \partial_y H_z(\mathbf{r},t) - \partial_z H_y(\mathbf{r},t)\\
\mu(\mathbf{r})\partial_t H_y(\mathbf{r},t) &= -\partial_z E_x(\mathbf{r},t)\\
\mu(\mathbf{r})\partial_t H_z(\mathbf{r},t) &= \partial_y E_x(\mathbf{r},t)
\end{aligned} \tag{1}$$

where $\mu(\mathbf{r})$ and $\varepsilon(\mathbf{r})$ represent relative permeability and permittivity, respectively. Note that field, time, and space quantities in (1) are unit-free and normalized as $t = c_0\tilde{t}/R$, $\mathbf{r} = \tilde{\mathbf{r}}/R$, $E_x = \tilde{E}_x/(H_0 Z_0)$, and $H_v = \tilde{H}_v/H_0$, $v \in \{y, z\}$, where, quantities with "$\sim$" represent physical fields, time, and space, R is reference length (m), H_0 is unit magnetic field strength (A/m), and $c_0 = (\mu_0\varepsilon_0)^{-1/2}$ (m/s) and $Z_0 = (\mu_0/\varepsilon_0)^{1/2}$ (ohms) are the speed of light and wave impedance in free space. To numerically solve (1), Ω_L is triangulated into N_e number of non-overlapping elements. On element k, $E_x(\mathbf{r},t)$ and $H_v(\mathbf{r},t)$, $v \in \{y, z\}$ are expanded as

$$\begin{aligned}
E_x(\mathbf{r},t) &\simeq \sum\nolimits_{i=1}^{N_p} E_x(\mathbf{r}_i,t)\ell_i(\mathbf{r})\\
&= \sum\nolimits_{i=1}^{N_p} E_{x,i}^k(t)\ell_i(\mathbf{r})\\
H_v(\mathbf{r},t) &\simeq \sum\nolimits_{i=1}^{N_p} H_v(\mathbf{r}_i,t)\ell_i(\mathbf{r})\\
&= \sum\nolimits_{i=1}^{N_p} H_{v,i}^k(t)\ell_i(\mathbf{r}).
\end{aligned} \tag{2}$$

Here, $\ell_i(\mathbf{r})$ are the pth-order interpolating Lagrange polynomials, $N_p = (p+1)(p+2)/2$ and $\mathbf{r}_i$ denote the number and the location of interpolating nodes, respectively [1]. $E_{x,i}^k(t)$ and $H_{v,i}^k(t)$, $v \in \{y, z\}$ are the unknown field samples to be determined. Inserting (2) into (1), testing the resulting equations with $\ell_i(\mathbf{r})$, and applying integration by parts twice yields

$$\begin{aligned}
\varepsilon^k \partial_t \mathbf{E}_x^k(t) &= \mathbf{D}_y^k \mathbf{H}_z^k(t) - \mathbf{D}_z^k \mathbf{H}_y^k(t) + (\mathbf{M}^k)^{-1}\mathbf{N}^k \mathbf{F}_{Ex}^k(t)\\
\mu^k \partial_t \mathbf{H}_y^k(t) &= -\mathbf{D}_z^k \mathbf{E}_x^k(t) + (\mathbf{M}^k)^{-1}\mathbf{N}^k \mathbf{F}_{Hy}^k(t)\\
\mu^k \partial_t \mathbf{H}_z^k(t) &= \mathbf{D}_y^k \mathbf{E}_x^k(t) + (\mathbf{M}^k)^{-1}\mathbf{N}^k \mathbf{F}_{Hz}^k(t)
\end{aligned} \tag{3}$$

for $k = 1, \ldots, N_e$. Here, superscript "k" represents quantities associated with element k, μ^k and ε^k are relative permeability and permittivity, which are assumed constant over element k; $\mathbf{E}_x^k(t)$ and $\mathbf{H}_v^k(t)$, $v \in \{y, z\}$ are $N_p \times 1$ vectors of unknown field samples; $\mathbf{D}_v^k$, $v \in \{y, z\}$, $\mathbf{N}^k$, and $\mathbf{M}^k$ are $N_p \times N_p$ differentiation, face, and mass matrices, respectively. Non-zero elements of these vectors and matrices are

$$\begin{aligned}
\left[\mathbf{E}_x^k(t)\right]_i &= E_{x,i}^k(t), \quad \left[\mathbf{H}_v^k(t)\right]_i = H_{v,i}^k(t)\\
\left[\mathbf{D}_v^k\right]_{ij} &= \partial_v \ell_j(\mathbf{r}_i), \quad v \in \{y, z\}\\
\left[\mathbf{M}^k\right]_{ij} &= \int_{\Omega^k} \ell_i(\mathbf{r})\ell_j(\mathbf{r})d\mathbf{r}\\
\left[\mathbf{N}^k\right]_{ij} &= \int_{\partial\Omega^k} \ell_i(\mathbf{r})\ell_j(\mathbf{r})d\mathbf{r}, \quad j \in \left\{j : \mathbf{r}_j \in \partial\Omega^k\right\}
\end{aligned} \tag{4}$$

for $i = 1, \ldots, N_p$ and $j = 1, \ldots, N_p$. Here, Ω^k is the support of element k and $\partial\Omega^k$ is its boundary. In (3), $\mathbf{F}_{Ex}^k(t)$, $\mathbf{F}_{Hy}^k(t)$, and $\mathbf{F}_{Hz}^k(t)$ are vectors of jump discontinuities between element k and its neighbors (numerical fluxes) [1]. Non-zero elements of these vectors are

$$\begin{aligned}
&\left[\mathbf{F}_{Ex}^k(t)\right]_{i'}\\
&\quad = Z^{-1}\left(Z^l\left(n_{z,i'}\Delta H_{y,i'}^k - n_{y,i'}\Delta H_{z,i'}^k\right) - \Delta E_{x,i'}^k\right)\\
&\left[\mathbf{F}_{Hy}^k(t)\right]_{i'}\\
&\quad = -n_{z,i'}Y^{-1}\left(n_{z,i'}\Delta H_{y,i'}^k - n_{y,i'}\Delta H_{z,i'}^k - Y^l\Delta E_{x,i'}^k\right)\\
&[\mathbf{F}_{Hz}^k(t)]_{i'}\\
&\quad = n_{y,i'}Y^{-1}\left(n_{z,i'}\Delta H_{y,i'}^k - n_{y,i'}\Delta H_{z,i'}^k - Y^l\Delta E_{x,i'}^k\right)
\end{aligned} \tag{5}$$

for $i' \in \left\{i : \mathbf{r}_i \in \partial\Omega^k \cap \partial\Omega^l,\ i = 1, \ldots, N_p\right\}$ and l is the index of any element neighboring element k. Here, $Z = Z^k + Z^l$, $Y = Y^k + Y^l$, $Z^v = 1/Y^v = (\mu^v/\varepsilon^v)^{1/2}$, $v \in \{k, l\}$, $\hat{\mathbf{n}}_{i'} = (n_{y,i'}, n_{z,i'})$ is the outward-pointing unit normal on $\partial\Omega^k$ at $\mathbf{r}_{i'}$, $\Delta E_{x,i'}^k = E_{x,i'}^k(t) - E_{x,j'}^l(t)$ and $\Delta H_{v,i'}^k = H_{v,i'}^k(t) - H_{v,j'}^l(t)$, $v \in \{y, z\}$, for $j' : \mathbf{r}_{j'} = \mathbf{r}_{i'}$, where j' runs through the indices of element l's nodes. It should be noted here that index l runs through indices of all neighbors of element k and (5) is valid for all of these elements.

It should be noted here that the numerical flux could be used for introducing excitation into the computation domain. Here, this is implemented via commonly used total field/scattered field (TF/SF) approach

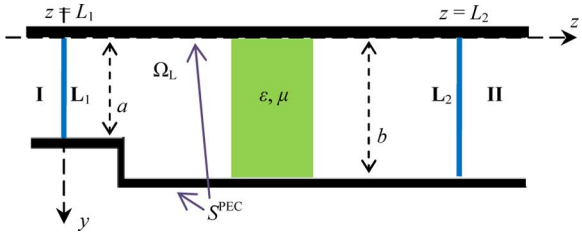

Fig. 1. Geometry of the model waveguide problem.

[1], [3], [9]. Let $E_x^{\mathrm{inc}}(\mathbf{r},t)$ and $H_v^{\mathrm{inc}}(\mathbf{r},t)$, $v \in \{y,z\}$, and $S^{\mathrm{TF/SF}}$ represent fields of an incident electromagnetic wave and the contour enclosing the TF region, where all inhomogeneities are located, respectively. To account for the difference in the fields on $S^{\mathrm{TF/SF}}$, numerical flux of the elements in contact with $S^{\mathrm{TF/SF}}$ are modified. This achieved by setting $\Delta E_{x,i'}^k = E_{x,i'}^k(t) - E_{x,j'}^l(t) \mp E_x^{\mathrm{inc}}(\mathbf{r}_{i'},t)$ and $\Delta H_{v,i'}^k = H_{v,i'}^k(t) - H_{v,j'}^l(t) \mp H_v^{\mathrm{inc}}(\mathbf{r}_{i'},t)$, $v \in \{y,z\}$, for $i' \in \left\{ i : \mathbf{r}_i \in \partial\Omega^k \cap \partial\Omega^l \cap S^{\mathrm{TF/TS}},\ i = 1,\ldots,N_p \right\}$ and $j' : \mathbf{r}_{j'} = \mathbf{r}_{i'}$ in (5); here the sign "$-$" should be selected if element k is in TF region, and "$+$" if it is in SF region [1], [3].

Numerical flux could also be used for accounting for PEC objects. Boundary conditions on S^{PEC} (surfaces of all PEC objects) are enforced by modifying the numerical flux of the elements in contact with S^{PEC}. This is achieved by setting in (5) $Z^l = Z^k$, $Y^l = Y^k$, $\Delta E_{x,i'}^k = 2E_{x,i'}^k(t)$ and $\Delta H_{v,i'}^k = 0$, $v \in \{y,z\}$, for $i' \in \left\{ i : \mathbf{r}_i \in \partial\Omega^k \cap S^{\mathrm{PEC}},\ i = 1,\ldots,N_p \right\}$ [1].

Finally, a few observations in regarding (1)–(5) are in order: (i) (1)–(5) are only derived for TE waves; extension to transverse magnetic (TM) waves is trivial. (ii) The time samples of $\mathbf{E}_x^k(t)$ and $\mathbf{H}_v^k(t)$, $v \in \{y,z\}$ are obtained by integrating the set of ordinary differential equations in (3). In this work, the fourth-order Runge-Kutta scheme is used for this purpose [1]; other time integration schemes could be used [1], [3]–[5] without any modifications on the scheme described above. (iii) Expressions of numerical flux in (5) are derived from the solution of the Riemann problem using upwind numerical flux formulation [1]. It should be noted that use of other flux formulations, e.g., central flux, would only affect (5) leaving the other equations untouched.

B. Time-Domain EACs and Their Discretization

The time-domain EACs are enforced on the virtual boundaries $\mathbf{L}_1$ and $\mathbf{L}_2$ to truncate the unbounded physical domain Ω into the bounded computation domain Ω_L (Fig. 1); they are analytically derived from the radiation conditions of the outgoing waves. The derivations of the EACs enforced on $\mathbf{L}_1$ and $\mathbf{L}_2$ follow the same mathematical steps. In what follows only the derivation of the EAC on $\mathbf{L}_1$ is summarized for brevity; details of the derivation can be found in [10]–[12].

In external homogeneous domain $\mathbf{I}$, electromagnetic field components satisfy the wave equation

$$\begin{aligned} \partial_t^2 U(\mathbf{r},t) &= \partial_y^2 U(\mathbf{r},t) + \partial_z^2 U(\mathbf{r},t), \quad \mathbf{r} \in \mathbf{I}, \quad t > 0 \\ U(\mathbf{r},0) &= \partial_t U(\mathbf{r},t)\big|_{t=0} = 0 \end{aligned} \tag{6}$$

where $U(\mathbf{r},t)$ represents any of the field components $E_x(\mathbf{r},t)$ or $H_v(\mathbf{r},t)$, $v \in \{y,z\}$. To solve (6), $U(\mathbf{r},t)$, is expanded in terms of modes:

$$U(\mathbf{r},t) = \sum\nolimits_{n=1}^{\infty} u_n(z,t) e_n(y), \quad \mathbf{r} \in \mathbf{I}. \tag{7}$$

Here, the mode amplitudes $u_n(z,t)$ and $U(\mathbf{r},t)$ are related by

$$u_n(z,t) = \int_0^a U(\mathbf{r},t) e_n(y) dy, \quad n = 1,2,\ldots,$$

a is the width of $\mathbf{I}$ (Fig. 1) and $e_n(y)$ are the transverse eigenfunctions. For TE field interactions, $e_n(y) = \sqrt{2/a}\sin(f_n y)$ with eigenvalues $f_n = n\pi/a$, $n = 1,2,\ldots$. $u_n(z,t)$ are then governed by the initial-value problem

$$\begin{aligned} \partial_t^2 u_n(z,t) &= \partial_z^2 u_n(z,t) - f_n^2 u_n(z,t), \quad z \le L_1, \quad t > 0 \\ u_n(z,0) &= \partial_t u_n(z,t)\big|_{t=0} = 0, \quad n = 1,2,\ldots. \end{aligned} \tag{8}$$

Fourier transforming (8) turns it into an inhomogeneous Cauchy problem that can be solved in the space of generalized functions. Inverse Fourier transforming this solution provides the solution of (8) in time domain. Enforcing this solution on the virtual boundary $\mathbf{L}_1$ provides

$$\begin{aligned} u_n(L_1,t) = \int_0^t J_0[f_n(t-t')]\ \partial_z u_n(z,t')\big|_{z=L_1}\, dt' \\ t \ge 0, \quad n = 1,2,\ldots \end{aligned}$$

Here, $J_0(\cdot)$ is the zeroth-order Bessel function. After a series of mathematical manipulations, the solution of (6) at $\mathbf{r}_{L1} = (y, L_1)$, $0 < y < a$, $U(\mathbf{r}_{L1},t)$, is reconstructed from $u_n(L_1,t)$ using (7). This provides the time-domain EAC on $\mathbf{L}_1$:

$$\begin{aligned} \partial_t U(\mathbf{r}_{L1},t) = {} & \partial_z U(\mathbf{r},t)\big|_{\mathbf{r}=\mathbf{r}_{L1}} \\ & - \sum\nolimits_{n=1}^{\infty} f_n e_n(y) \int_0^t \frac{J_1[f_n(t-t')]}{t-t'} \\ & \times \int_0^a U(\mathbf{r}'_{L1},t') e_n(y') dy' dt' \\ & 0 < y < a, t \ge 0 \end{aligned} \tag{9}$$

where $\mathbf{r}'_{L1} = (y', L_1)$ and $J_1(\cdot)$ is the first-order Bessel function. Similarly, the time-domain EAC on $\mathbf{L}_2$ can be derived:

$$\begin{aligned} \partial_t U(\mathbf{r}_{L2},t) = {} & -\partial_z U(\mathbf{r},t)\big|_{\mathbf{r}=\mathbf{r}_{L2}} \\ & - \sum\nolimits_{n=1}^{\infty} f_n e_n(y) \int_0^t \frac{J_1[f_n(t-t')]}{t-t'} \\ & \times \int_0^b U(\mathbf{r}'_{L2},t') e_n(y') dy' dt' \\ & 0 < y < b, t \ge 0 \end{aligned} \tag{10}$$

where b is the width of $\mathbf{II}$ (Fig. 1), $\mathbf{r}_{L2} = (y, L_2)$ and $\mathbf{r}'_{L2} = (y', L_2)$. Time-domain EACs in (9) and (10) establish relation between boundary values of the electromagnetic field components and their normal derivatives. Electromagnetic fields, which originate in Ω_L and arrive onto $\mathbf{L}_1$ and $\mathbf{L}_2$ are neither deformed nor reflected back into Ω_L; the fields acts as if they are being absorbed by $\mathbf{I}$ and $\mathbf{II}$ (by $\mathbf{L}_1$ and $\mathbf{L}_2$).

The time-domain EACs (9) in and (10) are discretized using a scheme that is fully consistent with the discretization of the Maxwell equations, which is carried out by the TD-DG-FEM. The scheme follows the same steps for (9) and (10), hence only the discretization of (9) is detailed step-by-step in what follows.

(i) The summation over n [the spatial harmonics in expansion (7)] is truncated to a finite number of terms, N_h. This finite number should be chosen in such a way that the fastest spatial variation (highest spectral content) of the fields passing through the virtual boundaries could be captured by the highest harmonic included in the summation. Spectral content of the fields depend on the properties of the excitation (frequency, location and shape of the source, etc.) as well as the geometry of the structure under analysis. For example, if the process under study involves intensive mode coupling or the excitation signal is wideband, then N_h should be set to rather big value, up to a few tens. On the other hand, e.g., for a single-mode waveguide, N_h could be set as small as five. It should be noted here that choosing N_h arbitrarily very large

might introduce unexpected errors in the solution since the discretization will not be able to resolve the spatial variation introduced by the higher harmonics.

(ii) Assume that discretization element m "touches" the virtual boundary $\mathbf{L}_1$. The field component $U(\mathbf{r}_{L1},t)$ and the eigenfunctions $e_n(y)$, $n=1,\ldots,N_h$, are sampled at element m's nodal points that reside on $\mathbf{L}_1$, i.e., at $\mathbf{r}_{i'}$ $i'\in\{i:\mathbf{r}_i\in\mathbf{L}_1,\ i=1,\ldots,N_p\}$. It should be emphasized here that $\mathbf{r}_i$, $i=1,\ldots,N_p$, are the interpolation nodes of the Lagrange basis functions [see (2)] defined on element m. These samples are stored in $N_s\times 1$ vectors $\mathbf{U}^m(t)$ and $\mathbf{e}_n^m$, where $N_s=p+1$ is the size of the set $i'\in\{i:\mathbf{r}_i\in\mathbf{L}_1,\ i=1,\ldots,N_p\}$, i.e., the number of element m's nodes that reside on $\mathbf{L}_1$. Note that index m runs through the indices of all elements that have nodes on $\mathbf{L}_1$.

(iii) The normal derivative operator "∂_z" is approximated from the samples of field values on $\mathbf{L}_1$ and in the vicinity of $\mathbf{L}_1$ using Lagrange interpolation. For this purpose the differentiation matrix of element m, $\mathbf{D}_z^m$, is used. The matrix $\mathbf{P}^m\mathbf{D}_z^m$ is applied to vectors of field samples $\hat{\mathbf{E}}_x^m(t)$ and $\hat{\mathbf{H}}_v^m(t)$, $v\in\{y,z\}$ to produce the samples of $\partial_z U(\mathbf{r},t)|_{\mathbf{r}=\mathbf{r}_{L1}}$. Here, $\mathbf{P}^m$ is a $N_s\times N_p$ sparse matrix, which chooses field samples at $\mathbf{r}_{i'}$, $i'\in\{i:\mathbf{r}_i\in\mathbf{L}_1, i=1,\ldots,N_p\}$; and the elements of $\hat{\mathbf{E}}_x^m(t)$ and $\hat{\mathbf{H}}_v^m(t)$, $v\in\{y,z\}$ are

$$\left[\hat{\mathbf{E}}_x^m(t)\right]_i=\begin{cases}[\mathbf{U}^m(t)]_j & \text{if } \mathbf{r}_i\in\mathbf{L}_1 \text{ and } \mathbf{r}_j=\mathbf{r}_i\\ [\mathbf{E}_x^m(t)]_i=E_{x,i}^m(t), & \text{otherwise}\end{cases}$$
$$\left[\hat{\mathbf{H}}_v^m(t)\right]_i=\begin{cases}[\mathbf{U}^m(t)]_j & \text{if } \mathbf{r}_i\in\mathbf{L}_1 \text{ and } \mathbf{r}_j=\mathbf{r}_i\\ [\mathbf{H}_v^m(t)]_i=H_{v,i}^m(t), & \text{otherwise}\end{cases}$$

for $i=1,\ldots,N_p$. It should be clear that in the above equations $\mathbf{U}^m(t)$ stores the exact boundary field samples for the corresponding field component. Thus, the multiplication $\mathbf{P}^m\mathbf{D}_z^m\hat{\mathbf{U}}^m(t)$ results in a $N_s\times 1$ vector, which stores the samples of $\partial_z U(\mathbf{r},t)|_{\mathbf{r}=\mathbf{r}_{L1}}$. Obviously, $\hat{\mathbf{U}}^m(t)$ represents any of $\hat{\mathbf{E}}_x^m(t)$ or $\hat{\mathbf{H}}_v^m(t)$, $v\in\{y,z\}$. Note that the approximation $\mathbf{P}^m\mathbf{D}_z^m\hat{\mathbf{U}}^m(t)$ has the same order of accuracy as the spatial discretization scheme of the TD-DG-FEM.

(iv) The integration over y' is approximated as a summation of numerical integrations each of which is computed using Gauss-Lobatto rule [14] on each element "touching" $\mathbf{L}_1$. On such an element indexed with m', Gauss-Lobatto rule uses the sampling nodes of Lagrange basis functions on $\mathbf{L}_1$, i.e., $\mathbf{r}_{i'}$, $i'\in\{i:\mathbf{r}_i\in\mathbf{L}_1,\ i=1,\ldots,N_p\}$, as quadrature points. The weights associated with $\mathbf{r}_{i'}$ are stored in an $N_s\times N_s$ diagonal matrix $\mathbf{w}^{m'}$. Note that Gauss-Lobatto rule has the same order of accuracy as the spatial discretization scheme of the TD-DG-DEM.

The above four steps yield the following semi-discrete equation:

$$\partial_t\mathbf{U}^m(t)=\mathbf{P}^m\mathbf{D}_z^m\hat{\mathbf{U}}^m(t)-\sum_{n=1}^{N_h}f_n\mathbf{e}_n^m\int_0^t\frac{J_1[f_n(t-t')]}{t-t'}\sum_{m'}\mathbf{w}^{m'}\mathbf{U}^{m'}(t')\mathbf{e}_n^{m'}dt' \quad (11)$$

where m and m' run through indices of all elements that have nodes on $\mathbf{L}_1$. Similarly, discretization of the time-domain EAC in (10) produces

$$\partial_t\mathbf{U}^m(t)=-\mathbf{P}^m\mathbf{D}_z^m\hat{\mathbf{U}}^m(t)-\sum_{n=1}^{N_h}f_n\mathbf{e}_n^m\int_0^t\frac{J_1[f_n(t-t')]}{t-t'}\sum_{m'}\mathbf{w}^{m'}\mathbf{U}^{m'}(t')\mathbf{e}_n^{m'}dt' \quad (12)$$

where now m and m' run through indices of all elements that have nodes on $\mathbf{L}_2$.

As described in Section II-A, the (discontinuous) field values on the nodes of the common edge of two neighboring discretization elements are "connected" via the numerical flux, see (5) and [1], [2]. The same argument holds true for the field values on the nodes shared by $\mathbf{L}_1$ (or $\mathbf{L}_2$) and a discretization element and these values can be "connected" using numerical flux. This is achieved by setting $\Delta E_{x,i'}^m=E_{x,i'}^m(t)-[\mathbf{U}^m(t)]_{j'}$ and $\Delta H_{v,i'}^m=H_{v,i'}^m(t)-[\mathbf{U}^m(t)]_{j'}$, $v\in\{y,z\}$, for $i'\in\{i:\mathbf{r}_i\in\mathbf{L}_1,\ i=1,\ldots,N_p\}$, j' : $\mathbf{r}_{j'}=\mathbf{r}_{i'}$ in (5). Here, m runs through the indices of all elements that have nodes on $\mathbf{L}_1$. It should be clear that in each equation $\mathbf{U}^m(t)$ stores the exact boundary field samples for the corresponding field component.

Finally several observations regarding (9)–(12) are in order: (i) (3), (11), and (12) form a coupled set of ordinary differential equations in unknown samples $\mathbf{E}_x^m(t)$, $\mathbf{H}_v^m(t)$, $v\in\{y,z\}$, and $\mathbf{U}^m(t)$. Time samples of these unknowns are obtained by integrating this coupled set of ordinary differential equations in time via the fourth order Runge-Kutta method [1]. (ii) The EACs (9) in and (10) are nonlocal (note the time integration/convolution over t') but this could be mitigated using analytical localization [10]–[12] without affecting the exactness of the EACs. (iii) The time convolution in (9) and (10) can be computed by any method, which provides the same level accuracy as the time integration used in computing the time samples of $\mathbf{E}_x^m(t)$, $\mathbf{H}_v^m(t)$, $v\in\{y,z\}$, and $\mathbf{U}^m(t)$. In this work, the Simpson's rule, which has the same order of accuracy as the fourth-order Runge-Kutta method is used for this purpose. It should be noted here that the computation of this time convolution could be significantly accelerated using blocked FFT-based techniques [10], [13], [15]–[17].

III. Numerical Results

In this section, the accuracy of the proposed TD-DG-FEM with EAC is compared to that of the TD-DG-FEM with PML and an approximate absorbing boundary condition (ABC) in computing transient fields on 2D waveguides. ABC considered here is the first-order Engquist-Majda condition [9], which enforces

$$\partial_t U(\mathbf{r}_{L1},t)=\partial_z U(\mathbf{r},t)|_{\mathbf{r}=\mathbf{r}_{L1}}$$
$$\partial_t U(\mathbf{r}_{L2},t)=-\partial_z U(\mathbf{r},t)|_{\mathbf{r}=\mathbf{r}_{L2}},\quad t\geq 0.$$

The discretization of derivative operators ∂_t and ∂_z is done following scheme described in Section II-A.

In all the examples, the normalization unit magnetic field $H_0=1\ \mathrm{A/m}$ and the reference length $R=1\ \mathrm{m}$. The time signature of the excitation is a modulated Gaussian pulse represented with $G(t)=e^{-(t-t_0)^2/4\alpha^2}\cos[\kappa(t-t_0)]$, where t_0, α, and κ are the pulse's delay, width and modulation frequency, respectively. The values of these parameters are set to $t_0=3$, $\alpha=0.36$, and $\kappa=15$. For simulations with TD-DG-FEM with PML, the PML parameter, $\sigma(z)$, raises cubically within the PML domain from zero up to 20 and is zero in the computation domain, see [3], [5]. To quantify the accuracy of the methods compared, the global absolute L^2 error,

$$err^{\mathrm{sim}}(t)=\sqrt{\frac{1}{N_e}\sum_{k=1}^{N_e}\int_{\Omega k}\left|E_x^{\mathrm{sim}}(\mathbf{r},t)-E_x^{\mathrm{PEC}}(\mathbf{r},t)\right|^2 d\mathbf{r}} \quad (13)$$

is computed in all numerical experiments. Here, $E_x^{\mathrm{sim}}(\mathbf{r},t)$, $\mathrm{sim}=\{\mathrm{EAC},\ \mathrm{ABC},\ \mathrm{PML}\}$ represents the electric field solution obtained using TD-DG-FEM with EAC, ABC, and PML. The reference electric field solution, $E_x^{\mathrm{PEC}}(\mathbf{r},t)$, is obtained using the same TD-DG-FEM on a computation domain with PEC walls, which is large enough so that within the duration of the simulation no reflection comes back into the computation domain, where $err^{\mathrm{sim}}(t)$ is computed. This approach allows for quantification of the error only caused by the method (EAC, ABC, or PML) used to truncate the physical domain. The TD-DG-FEM that is used for computing $E_x^{\mathrm{PEC}}(\mathbf{r},t)$ is conveniently named as "TD-DG-FEM with PEC" in the remainder of the section.

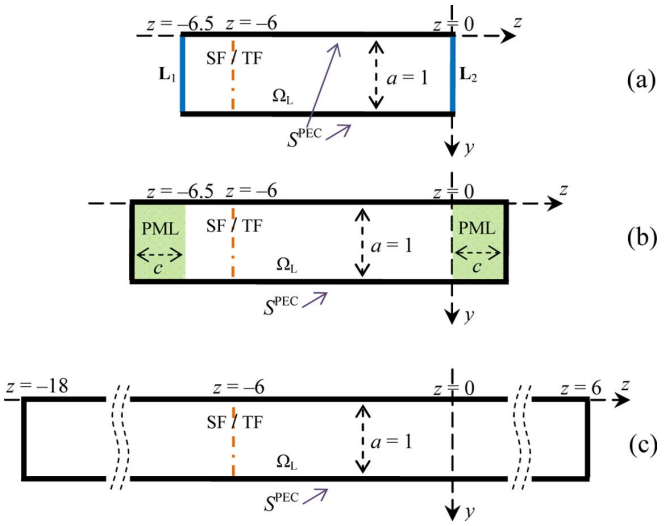

Fig. 2. (a) Computation domain with EAC and ABC truncation. (b) Computation domain with PML truncation. (c) Computation domain for reference solution.

TABLE I
TIME STEP SIZE FOR DIFFERENT POLYNOMIAL ORDERS

p	Δt
2	0.00756
3	0.00509
4	0.00359
5	0.00265
6	0.00203
7	0.00159
8	0.00129
9	0.00106
10	0.00089

A. Open-Ended Waveguide

The first structure considered is a 2D waveguide open at both ends (Fig. 2). The sizes of computation domains for simulations with TD-DG-FEM using EAC and ABC, PML, and PEC are $[0,1]\times[-6.5,0]$, $[0,1]\times[-6.5-c,c]$, and $[0,1]\times[-18,6]$, respectively. The thickness of PML, c, is set to two different values: 1 and 2. The virtual boundaries $\mathbf{L}_1$ and $\mathbf{L}_2$ are located at $z=L_1=-6.5$ and $z=L_2=0$, respectively. The average triangular mesh size is around 0.05 for all simulations; this results in $N_e=5200$ elements for the computation domains of TD-DG-FEM with EAC and ABC. The excitation is implemented via TF/SF approach; the TF/SF boundary is placed at $\mathbf{r}_e=(y,-6)$, $0<y<1$, (Fig. 2) and the excitation fields are $E_x^{\rm inc}(\mathbf{r}_e,t)=H_y^{\rm inc}(\mathbf{r}_e,t)=G(t)\sin(\pi y)$. Note that these fields excite only the first waveguide mode propagating in $+z$ direction. Since higher-order modes are not excited, the number of EAC harmonics is set to a rather low value, $N_h=7$. The order of interpolating polynomials, p, is changed from 2 to 10; for a given p, all four simulations with TD-DG-FEM using EAC, ABC, PML, and PEC use the same Δt (Table I). The duration of all simulations is $T=14$.

$E_x^{\rm PEC}(\mathbf{r},t)$ and $E_x^{\rm sim}(\mathbf{r},t)$ and $err^{\rm sim}(T)$, sim $=\{$EAC, ABC, PML$\}$, are computed for every $p=\{2,\ldots,10\}$. Fig. 3 plots $err^{\rm sim}(T)$, sim $=\{$EAC, ABC, PML$\}$, vs. p. Note that at $T=14$ the only fields present in the computation domain are the fields reflected from $\mathbf{L}_1$ and $\mathbf{L}_2$ or the PML; hence $err^{\rm sim}(T)$, sim $=\{$EAC, ABC, PML$\}$, provide a very good measure for the accuracy of EAC, ABC, and PML truncations. It is clearly seen from Fig. 3 that the accuracy of ABC and PML stays almost constant and

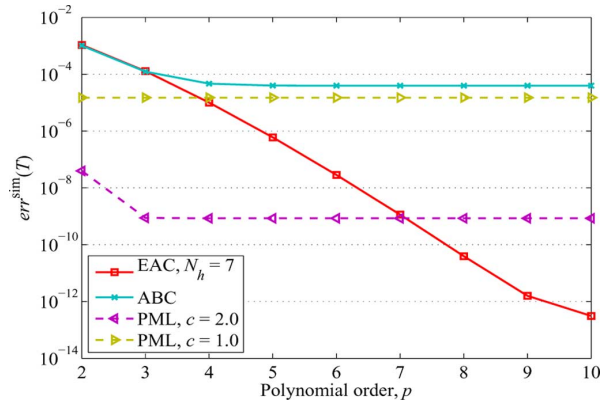

Fig. 3. $err^{\rm sim}(T)$, sim $=\{$EAC, ABC, PML$\}$ vs. p. $T=14$ is the duration of the simulation.

does not increase with p even though this constant value for thick $(c=2)$ PML is quite high (around 10^{-9}). This means that for higher values of p the overall accuracy of the solution is bounded by the error introduced due to the truncation of the physical domain by ABC and PML. For smaller values of p, PML accuracy becomes unnecessarily high since the overall accuracy of the solution is bounded by the error of TD-DG-FEM discretization. On the other hand, the accuracy of EAC increases with p and reaches around 10^{-13} for $p=10$. This is expected since the discretization of the EACs is fully consistent with the discretization used by the TD-DG-FEM itself. (Accuracy of TD-DG-FEM also increases with p.) It is clear from the behavior of $err^{\rm EAC}(T)$ that EAC truncation does not put a restriction on the accuracy of the solution.

It should be noted here that, in this example, the fields arrive normally onto $\mathbf{L}_1$ and $\mathbf{L}_2$ and PML; normal incidence is the "best case scenario" (highest accuracy) of PML and ABC truncation [3], [5], [9]. In the next Section IV, an example, where fields are not normally incident on the truncation surfaces, is considered to further demonstrate the effectiveness of the EAC and the proposed discretization scheme.

B. Waveguide Closed at One End

The structure considered in this section is a 2D waveguide, which is short-circuited at one end (Fig. 4). The sizes of computation domains for simulations with TD-DG-FEM using EAC and ABC, PML, and PEC are $[0,2]\times[-2,0]$, $[0,2]\times[-2,c]$, and $[0,2]\times[-2,11]$, respectively. The virtual boundary $\mathbf{L}_2$ is located at $z=L_2=0$. The thickness of PML, c, is set to two different values: 1 and 2. The average triangular mesh size is around 0.05 for all simulations; this results in $N_e=3200$ elements for the computation domains of TD-DG-FEM with EAC and ABC. The waveguide is excited by an electric-field soft source placed at $\mathbf{r}_e=(1,-1)$; its amplitude is $E_x^{\rm inc}(\mathbf{r}_e,t)=G(t)$. Note that, unlike the previous example, higher order propagating modes are excited. To demonstrate the influence of the number of harmonics, N_h, on the accuracy, EACs constructed using three different values of N_h, $N_h=\{13,15,20\}$, are considered. The order of interpolating polynomials, p, is changed from 2 to 10; for a given p, all four simulations with TD-DG-FEM using EAC, ABC, PML, and PEC use the same Δt (Table I). The duration of all simulations is $T=20$. This duration of simulation allows the fields to pass a few times even through the thick $(c=2)$ PML layer.

$E_x^{\rm PEC}(\mathbf{r},t)$ and $E_x^{\rm sim}(\mathbf{r},t)$ and $err^{\rm sim}(t)$, sim $=\{$EAC, ABC, PML$\}$, are computed for every $p=\{2,\ldots,10\}$. Fig. 5 plots $err^{\rm sim}(T)$, sim $=\{$EAC, ABC, PML$\}$, vs. p. It is clearly shown that the accuracy of ABC and PML stays constant and does not increase with p. These constants for ABC, and thin and thick

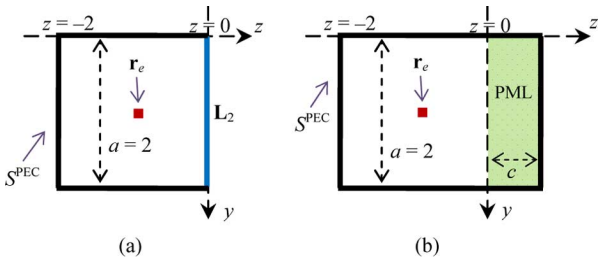

Fig. 4. (a) Computation domain with EAC and ABC truncation. (b) Computation domain with PML truncation.

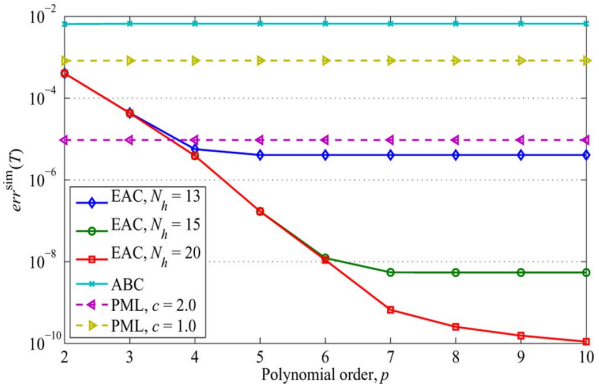

Fig. 5. $err^{\mathrm{sim}}(T)$, $\mathrm{sim} = \{\mathrm{EAC},\ \mathrm{ABC},\ \mathrm{PML}\}$ vs. p. $T = 20$ is the duration of the simulation.

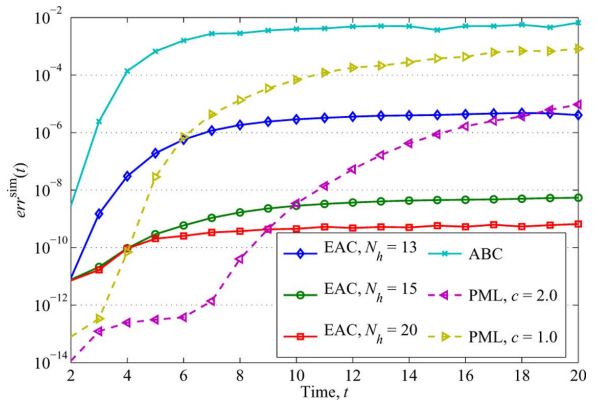

Fig. 6. $err^{\mathrm{sim}}(t)$, $\mathrm{sim} = \{\mathrm{EAC},\ \mathrm{ABC},\ \mathrm{PML}\}$ vs. t. Polynomial order is fixed as $p = 7$.

PML are around 10^{-2}, and 10^{-3} and 10^{-5}, respectively. A decrease in the accuracy compared to the previous example is expected since the fields are not only normally incident on the PML. On the other hand, the EAC accuracy exhibits the same dependence on p as in the previous example, provided that the number of harmonics, N_h, used in discretized EAC is high enough. The EAC error is as small as 10^{-10} for $p = 10$ and $N_h = 20$.

To demonstrate how the error of EAC, ABC, and PML changes during the simulation, Fig. 6 plots $err^{\mathrm{sim}}(t), \mathrm{sim} = \{\mathrm{EAC},\ \mathrm{ABC},\ \mathrm{PML}\}$, vs. t computed for $p = 7$. It is clearly seen that the EAC error stabilizes over time while the PML errors continue to grow.

For this example, for all values of p, CPU times required by the TD-DG-FEM using PML with $c = 1$ and $c = 2$ are approximately 1.8 and 2.6 longer that those required by the TD-DG-FEM using EAC with $N_h = 20$, respectively. It should be noted here that decreasing N_h to 13 or 15 reduces the overall CPU time only slightly since the cost of computations associated with EAC is already considerably smaller than that of the computations associated with TD-DG-FEM. For this example, the discretized temporal convolutions present in (11) and (12) are accelerated using the blocked-FFT scheme described in [10], [13], [15]–[17] without introducing any additional numerical errors.

IV. Conclusion

A scheme for rigorously discretizing the time-domain EACs and coupling the resulting equations to 2D Maxwell equations, which are discretized by the TD-DG-FEM is presented. Numerical results demonstrate that the accuracy of the EAC discretization increases with the order of the spatial basis functions used in TD-DG-FEM; and that the method used in the truncation of the computation domain does no longer limit the overall accuracy of the solution.

Extensions of the proposed scheme, which allow the use of vector basis functions in the spatial discretization and discretization of three-dimensional EACs enforced on spherical surfaces, are underway.

References

[1] J. S. Hesthaven and T. Warburton, *Nodal Discontinuous Galerkin Methods*. New York: Springer, 2008.

[2] B. Cockburn, S. Hou, and C.-W. Shu, "The Runge-Kutta local projection discontinuous Galerkin finite element method for conservation laws IV: The multidimensional case," *Math. Comp.*, vol. 54, no. 190, pp. 545–581, Apr. 1990.

[3] M. Liu, K. Sirenko, and H. Bagci, "An efficient discontinuous Galerkin finite element method for highly accurate solution of Maxwell equations," *IEEE Trans. Antennas Propag.*, vol. 60, no. 8, pp. 3992–3998, Aug. 2012.

[4] M. Liu and H. Bagci, "A new highly accurate time integration scheme for DG-FEM," in *Proc. 5th Eur. Conf. Antennas and Propagation*, Rome, Italy, 2011, pp. 3213–3215.

[5] J. Niegemann, M. König, K. Stannigel, and K. Busch, "Higher-order time-domain methods for the analysis of nano-photonic systems," *Photon. Nanostruct. Fundam. Appl.*, vol. 7, pp. 2–11, Sep. 2009.

[6] T. Hagstrom and T. Warburton, "High-order radiation boundary conditions for time-domain electromagnetics using an unstructured discontinuous Galerkin method," in *Proc. 2nd MIT Conf. Computational Fluid and Solid Mechanics*, 2003, pp. 1358–1363.

[7] T. Hagstrom, T. Warburton, and D. Givoli, "Radiation boundary conditions for time-dependent waves based on complete plane wave expansions," *J. Comp. Appl. Math.*, vol. 234, pp. 1988–1995, Aug. 2010.

[8] J. P. Berenger, "A perfectly matched layer for the absorption of electromagnetic waves," *J. Comput. Phys.*, vol. 114, pp. 185–200, Oct. 1994.

[9] A. Taflove and S. C. Hagness, *Computational Electrodynamics: The Finite-Difference Time-Domain Method*, 3rd ed. Boston: Artech House, 2005.

[10] K. Sirenko, V. Pazynin, Y. Sirenko, and H. Bagci, "An FFT-accelerated FDTD scheme with exact absorbing conditions for characterizing axially symmetric resonant structures," *Progress Electromagn. Res.*, vol. 111, pp. 331–364, Jan. 2011.

[11] K. Sirenko and Y. Sirenko, "Exact "absorbing" conditions in the initial boundary-value problems of the theory of open waveguide resonators," *Comp. Math. Math. Phys.*, vol. 45, no. 3, pp. 490–506, Mar. 2005.

[12] Y. K. Sirenko, S. Strom, and N. P. Yashina, *Modeling and Analysis of Transient Processes in Open Resonant Structures. New Methods and Techniques*. Berlin, Germany: Springer, 2007.

[13] K. Sirenko and H. Bagci, "An FDTD method with FFT-accelerated exact absorbing boundary conditions," in *Proc. IEEE Int. Symp. Antennas and Propagation (APSURSI)*, Spokane, WA, 2011, pp. 2315–2318.

[14] *Handbook of Mathematical Functions*, M. Abramowitz and I. A. Stegun, Eds. New York: Dover, 1972, pp. 887–888.

[15] H. Bagci, A. E. Yilmaz, and E. Michielssen, "An FFT-accelerated time-domain multiconductor transmission line simulator," *IEEE Trans. Electromagn. Compat.*, vol. 52, no. 1, pp. 199–214, Feb. 2010.

[16] H. Bagci, A. E. Yilmaz, J.-M. Jin, and E. Michielssen, "Fast and rigorous analysis of EMC/EMI phenomena on electrically large and complex cable-loaded structures," *IEEE Trans. Electromagn. Compat.*, vol. 49, no. 2, pp. 361–381, May 2007.

[17] H. Bagci, A. E. Yilmaz, V. Lomakin, and E. Michielssen, "Fast solution of mixed-potential time-domain integral equations for half-space environments," *IEEE Trans. Geosci. Remote Sensing*, vol. 43, no. 2, pp. 269–279, Feb. 2005.